



Evaluation of super-resolution performance of the K2 electron-counting camera using 2D crystals of aquaporin-0



Po-Lin Chiu^{a,1}, Xueming Li^{b,2,1}, Zongli Li^{a,c}, Brian Beckett^d, Axel F. Brilot^d, Nikolaus Grigorieff^e, David A. Agard^{b,f}, Yifan Cheng^{b,*}, Thomas Walz^{a,c,*}

^a Department of Cell Biology, Harvard Medical School, 240 Longwood Avenue, Boston, MA 02115, USA

^b The Keck Advanced Microscopy Laboratory, Department of Biochemistry and Biophysics, University of California San Francisco, 600 16th Street, San Francisco, CA 94158, USA

^c The Howard Hughes Medical Institute, Harvard Medical School, 240 Longwood Avenue, Boston, MA 02115, USA

^d Department of Biochemistry, Rosenstiel Basic Medical Sciences Research Center, Brandeis University, 415 South Street, Waltham, MA 02454, USA

^e Janelia Research Campus, 19700 Helix Drive, Ashburn, VA 20147, USA

^f The Howard Hughes Medical Institute, University of California San Francisco, 600 16th Street, San Francisco, CA 94158, USA

ARTICLE INFO

Article history:

Received 29 June 2015

Received in revised form 21 August 2015

Accepted 25 August 2015

Available online 28 August 2015

Keywords:

Direct electron detection device camera

Electron counting

Super-resolution

Two-dimensional crystal

ABSTRACT

The K2 Summit camera was initially the only commercially available direct electron detection camera that was optimized for high-speed counting of primary electrons and was also the only one that implemented centroiding so that the resolution of the camera can be extended beyond the Nyquist limit set by the physical pixel size. In this study, we used well-characterized two-dimensional crystals of the membrane protein aquaporin-0 to characterize the performance of the camera below and beyond the physical Nyquist limit and to measure the influence of electron dose rate on image amplitudes and phases.

© 2015 Elsevier Inc. All rights reserved.

1. Introduction

One of the most exciting technological breakthroughs in cryo-electron microscopy (cryo-EM) in recent years has been the development and application of complementary metal-oxide-semiconductor (CMOS)-based direct electron detection device (DDD) cameras (Faruqi and McMullan, 2011). The detective quantum efficiency (DQE) of these cameras is significantly higher, at both low and high spatial frequency, than those of the more traditionally used image recording media, photographic film and scintillator-based digital cameras such as charge-coupled device (CCD) cameras (Li et al., 2013a; McMullan et al., 2009a,b). A number of recent studies have characterized DDD cameras and demonstrated that these cameras are superb for high-resolution

cryo-EM (Bammes et al., 2012; Li et al., 2013a; McMullan et al., 2009a; Milazzo et al., 2011; Ruskin et al., 2013). The high DQE at high spatial frequency helps retain high-resolution information while the high DQE at low spatial frequency improves the image contrast needed for particle detection and alignment. The improved DQE makes it possible to record images of frozen-hydrated biological samples with sufficient contrast using a smaller defocus than previously required for imaging on photographic film or scintillator-based cameras. The high output frame rate of DDD cameras also enables recording of dose-fractionated image stacks (movies), and the correction of motion-induced image blurring (Bai et al., 2013; Campbell et al., 2012; Li et al., 2013a). The application of DDD cameras and the associated dose-fractionation movie technology has resulted in a number of high-resolution single-particle cryo-EM three-dimensional (3D) reconstructions at near-atomic resolution (e.g., Allegretti et al., 2014; Amunts et al., 2014; Campbell et al., 2012; Li et al., 2013a, b; Liao et al., 2013).

Among several commercially available DDD cameras, the K2 Summit camera from Gatan was the first one that had the capability of counting individual electron events in a practical manner (Li et al., 2013a). By identifying primary electron events, the electron counting process nearly doubles low-resolution DQE (Li et al.,

* Corresponding authors at: Department of Biochemistry and Biophysics, University of California San Francisco, 600 16th Street, San Francisco, CA 94158, USA (Y. Cheng), Department of Cell Biology, Harvard Medical School, 240 Longwood Avenue, Boston, MA 02115, USA (T. Walz).

E-mail addresses: ycheng@ucsf.edu (Y. Cheng), twalz@hms.harvard.edu (T. Walz).

¹ These authors contributed equally; listed alphabetically.

² Present address: Center for Structural Biology, School of Life Sciences, Tsinghua University, Beijing 100084, China.

2013a). It also removes Landau noise, which is generated from the statistical deposition of energy by the primary electrons. Counting also eliminates the readout noise and therefore, there is no penalty when the total dose is fractionated into multiple subframes. The signal cluster of each primary electron event can be further analyzed to identify its centroid, allowing its entry point to be assigned to a quadrant of the physical pixel. While the principle of centroiding is the same as the method used in light microscopy (Shroff et al., 2007), the exact algorithm used by the K2 Summit camera is proprietary information. However, much of the key behavior was deduced by direct analysis (Li et al., 2013b). In such super-resolution images, the effective Nyquist frequency is extended to twice the physical Nyquist frequency of the camera, thereby reducing aliasing. Counting and centroiding result in a significant improvement in image quality and resolution. For a detailed comparison of the K2 camera with other currently available DDD cameras, see Ruskin et al. (2013) and McMullan et al. (2014).

A potential drawback of a counting camera is that the usable dose rate on the camera is limited by coincidence loss, i.e., when more than one electron strikes the same pixel or neighboring pixels in the same frame, only one is counted and the additional electrons are ignored. While the K2 camera has a very high internal frame rate (400 frames/s), coincidence loss becomes significant at dose rates above $\sim 8 \text{ e}^-/\text{pixel/s}$ (Li et al., 2013a). Counting images have now resulted in numerous 3D maps at near-atomic resolution including the recent map of β -galactosidase at a nominal resolution of 2.2 Å (Bartesaghi et al., 2015), but the data have largely been recorded under conditions for which the obtained resolutions are not substantially better than the physical Nyquist of the camera. Thus, it is not clear if the centroiding operation accurately preserves image amplitude and phase information.

In this work, we used two-dimensional (2D) crystals of aquaporin-0 (AQP0) as a test specimen to further characterize the influence of dose rate and centroiding on image phases and amplitudes, particularly beyond the physical Nyquist frequency. We recorded images of 2D crystals at different magnifications and different dose rates. Phase errors from merging the images recorded under different conditions provide a quantitative measure to assess the influence of dose rate and centroiding on image phases. We demonstrate that imaging with the K2 Summit camera operated in super-resolution mode does not increase the phase error of merged reflections, suggesting that the phase error introduced by centroiding and coincidence loss at low dose rates, if there is any, is sufficiently small and tolerable for high-resolution imaging. We find, however, that in images recorded at high dose rates in super-resolution mode, coincidence loss results in large amplitude errors in the low-resolution range (Li et al., 2013b). (This is likely also the case for images recorded at high dose rates in counting mode).

Centroiding quadruples the total number of usable pixels of the camera. A global motion correction algorithm can correct beam-induced motion with sub-physical pixel precision and restore image resolution (measured by amplitude) to beyond the physical Nyquist frequency (Li et al., 2013a). Although the DQE drops significantly beyond the physical Nyquist frequency, the use of super-resolution pixels could potentially further increase the efficiency of cryo-EM data acquisition. While there may be other factors that limit the resolution of single-particle cryo-EM images recorded at low magnification, we demonstrate here that images of 2D crystals recorded with the K2 Summit camera preserve phase information to near the super-resolution Nyquist frequency. Furthermore, we performed dose fractionation experiments to investigate if the loss of structural integrity of AQP0 crystals due to radiolysis under the electron beam depends on the timing of the fractional doses.

2. Materials and methods

2.1. Preparation of AQP0 2D crystals

AQP0 was purified and crystallized as described previously (Gonen et al., 2004). Briefly, membranes were isolated from the core of sheep lenses (purchased from Wolverine Packing Company, Detroit, MI), washed, and solubilized with 4% (w/v) *n*-octyl- β -D-glucoside (OG) (Affymetrix). The insoluble fraction was removed by centrifugation at 300,000g for 45 min at 4 °C, and the supernatant was run over a Mono Q ion-exchange column (GE Healthcare). Bound proteins were eluted with 150 mM NaCl in 1.2% (w/v) OG and 10 mM Tris-Cl, pH 8.0. Peak fractions were pooled and run over a Superose 12 column (GE Healthcare) in 1.2% (w/v) OG, 10 mM Tris-HCl, pH 8.0, and 100 mM NaCl. Purified AQP0 was first mixed with a 1:2 (mol/mol) mixture of sphingomyelin and cholesterol (Avanti Polar Lipids) at a lipid-to-protein ratio (LPR) of 0.2 or with a 4:1 (w/w) mixture of dimyristoyl phosphatidylethanolamine (DMPE) and dimyristoyl phosphatidylglycerol (DMPG) (Avanti Polar Lipids) at an LPR of 0.6. Both mixtures were dialyzed against 10 mM MES, pH 6.0, 30 mM MgCl₂, 100 mM NaCl, and 0.05% NaN₃ at 37 °C for one week with daily buffer exchanges.

2.2. Grid preparation and data collection

AQP0 2D crystals were prepared on molybdenum grids with 7% (w/v) trehalose solution using a modified version of the carbon sandwich method (Gyobu et al., 2004; Hite et al., 2010b), and the grids were frozen in liquid nitrogen. The grids were transferred into a Tecnai F20 electron microscope (FEI Company, Hillsborough, OR) using an Oxford CT3500 side-entry cryo-specimen holder. Data on the Tecnai F20 were collected at an acceleration voltage of 200 kV, and a nominal defocus range of -0.5 to $-0.8 \mu\text{m}$. Crystals were also imaged with a Polara electron microscope (FEI Company, Hillsborough, OR) operated at an acceleration voltage of 300 kV, using a nominal defocus range of -0.2 to $-0.5 \mu\text{m}$. Data were collected using low-dose procedures and K2 Summit cameras (Gatan Inc., Pleasanton, CA). The physical pixel size of the K2 Summit camera is 5 μm . The chip size of the camera sensor is 3838 \times 3710 pixels, and images were reduced to a square size of 3710 \times 3710 pixels.

Dose-fractionated image stacks were recorded in super-resolution mode following established procedures (Li et al., 2013a). To set the desired dose rate, first gain and dark references were prepared in the linear and super-resolution modes, and then the “Profile” option of the Gatan Digital Micrograph software was used to adjust the beam intensity and set up the counting rate using an area containing a 2D crystal. On the Tecnai F20, for images collected at a calibrated magnification of 40,410 \times (nominal magnification of 29,000 \times), a dose rate of 8 counts/pixel/s (5.2 counts/Å²/s) was used. Frames were read out every 150 ms and 27 frames were collected, resulting in an exposure time of 4.05 s and a total dose of 21 counts/Å². For images collected at a calibrated magnification of 15,858 \times (nominal magnification of 11,500 \times), a dose rate of 10 counts/pixel/s (1.04 counts/Å²/s) was used. Frames were read out every 400 ms and 50 frames were collected, resulting in an exposure time of 20 s and a total dose of 20 counts/Å². On the Polara, dose-fractionated images in super-resolution mode were recorded at liquid nitrogen temperature at a calibrated magnification of 50,926 \times (nominal magnification of 39,000 \times), and a dose rate of 8 counts/pixel/s (8.33 counts/Å²/s) was used. Frames were read out every 150 ms and 16 frames were collected, resulting in an exposure time of 2.4 s and a total dose of 20 counts/Å².

Image stacks used to study dose-dependent radiation damage were recorded on a K2 Summit camera mounted on an FEI TF30 microscope operated at 300 kV, and using a calibrated magnification of $50,637\times$ (nominal magnification of $39,000\times$), giving a super-resolution pixel size on the specimen level of 0.494 \AA . All movies contained a total of 20 frames with $2.5\text{ counts/\AA}^2/\text{frame}$, of which the final two frames were discarded. For dataset “6 parts”, the image stacks were recorded in six bursts containing three frames each. Bursts were separated by pauses of $\sim 30\text{ s}$. Image stacks for dataset “18 parts” were recorded as 18 individual frames separated by $\sim 15\text{ s}$ pauses.

2.3. Image processing

The UCSF Image software was used to collect dose-fractionated image stacks and to align the frames prior to summing them up as described (Li et al., 2013a). The drift-corrected images of the AQP0 2D crystals were processed and merged using the *2dx* software (Gipson et al., 2007a,b), which is based on the MRC image-processing package (Crowther et al., 1996). The 2D crystals have lattice parameters of $a = 65.5\text{ \AA}$, $b = 65.5\text{ \AA}$, and $\gamma = 90^\circ$, and *p422* plane symmetry. The crystal lattices were unbent, and the images were corrected for the contrast-transfer function (CTF), which was determined with CTFIND3 (Mindell and Grigorieff, 2003). For all datasets, the best seven images of well-diffracting crystals were merged. The merging statistics in resolution ranges are listed in Supplementary Tables 1–11.

Image stacks recorded to assess dose-dependent radiation damage were processed as described (Li et al., 2013a). Frames of movies that included pauses were combined into single stacks for frame alignment. For each image series, six drift-corrected frame averages were calculated from groups of three frames each. Processing of the averages using the MRC image processing suite (Crowther et al., 1996) yielded lists of indexed amplitudes that were tabulated according to resolution shell and total dose received. Using only reflections with IQ values of 4 and lower (corresponding to an SNR of about 1.8 and higher), average amplitude ratios were calculated with respect to the measurement corresponding to a total dose of 7.5 counts/\AA^2 , as well as the standard errors of the ratios. The results are plotted in Fig. 7.

3. Results and discussion

3.1. Imaging AQP0 2D crystal

AQP0 forms well-ordered 2D crystals with a variety of lipids (Gonen et al., 2004, 2005; Hite et al., 2010a). For this study, we used 2D crystals of AQP0 reconstituted with lipid mixtures of 1:2 (mol/mol) sphingomyelin and cholesterol, and 4:1 (w/w) phosphatidylethanolamine (PE) and phosphatidylglycerol (PG). The lattice parameters as well as the order of these 2D crystals were the same as those of AQP0 2D crystals obtained before with other lipids.

Dose-fractionated image stacks of AQP0 2D crystals were first recorded with a K2 Summit camera mounted on an FEI Tecnai F20 electron microscope operated at an acceleration voltage of 200 kV. At a calibrated magnification of $40,410\times$, the physical and super-resolution pixel sizes on the specimen level are 1.24 \AA and 0.62 \AA , corresponding to physical and super-resolution Nyquist frequencies of $1/(2.48\text{ \AA})$ and $1/(1.24\text{ \AA})$, respectively. After binning over 2×2 super-resolution pixels and performing motion correction (Li et al., 2013a), power spectra showed Thon rings to about 2.9 \AA resolution (Fig. 1A). After lattice unbending in *2dx* (Gipson et al., 2007a), intensity quotient (IQ) plots showed diffraction spots with IQ values of 3 (corresponding to a peak-to-background ratio of 2.3; Henderson et al., 1986) up to a resolution of about 3.0 \AA (Fig. 1B). The best seven images were merged in *2dx* (Gipson et al., 2007b), and the merging statistics indicate that the phase information is reliable to a resolution of 3.4 \AA (90° is random) (Supplementary Table 1). The merged projection map at 3.4 \AA resolution is shown in Fig. 1C and D.

We also imaged AQP0 2D crystals with a K2 Summit camera mounted on an FEI Polara electron microscope operated at an acceleration voltage of 300 kV. The Polara employs an internal cartridge system, which is considerably more stable than the side-entry cryo-specimen holder used with the Tecnai F20. In addition, higher acceleration voltages (1) reduce the scattering cross-section, resulting in fewer multiple-scattering events, (2) give a lower Ewald sphere curvature, thus extending the breakdown limit of the central projection theorem (Zhang and Zhou, 2011), and (3) allow for a better performance of the DDD camera (Ruskin et al.,

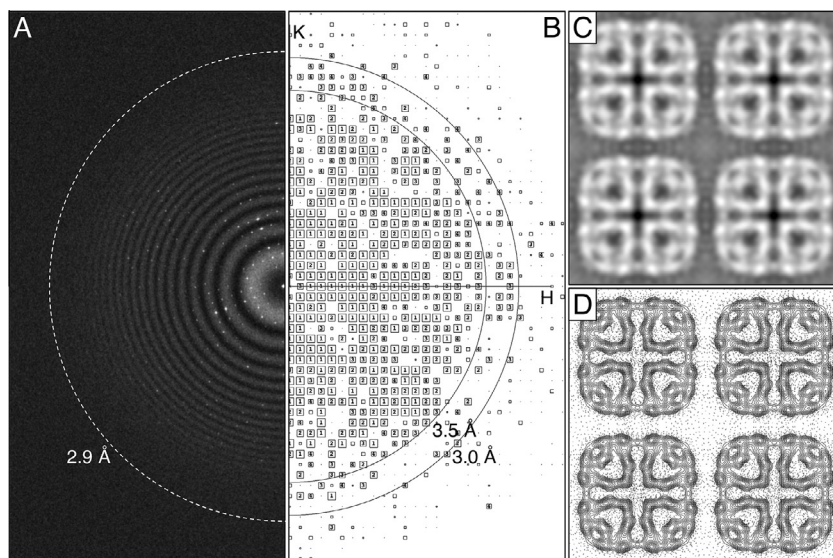


Fig. 1. Imaging of AQP0 2D crystals with a K2 Summit camera mounted on an FEI Tecnai F20 electron microscope operated at 200 kV. (A) The power spectrum of a typical drift-corrected image recorded at a calibrated magnification of $40,410\times$ after binning over 2×2 pixels shows Thon rings to a resolution of about 2.9 \AA (indicated by dashed ring). (B) The IQ plot of a typical AQP0 2D crystal after lattice unbending shows IQ = 3 spots to a resolution better than 3 \AA . (C) Projection map of AQP0 at 3.4 \AA resolution obtained by merging the best seven images. (D) Projection map shown as contour plot. Panels C and D show four AQP0 unit cells, each with a side length of $a = b = 65.5\text{ \AA}$.

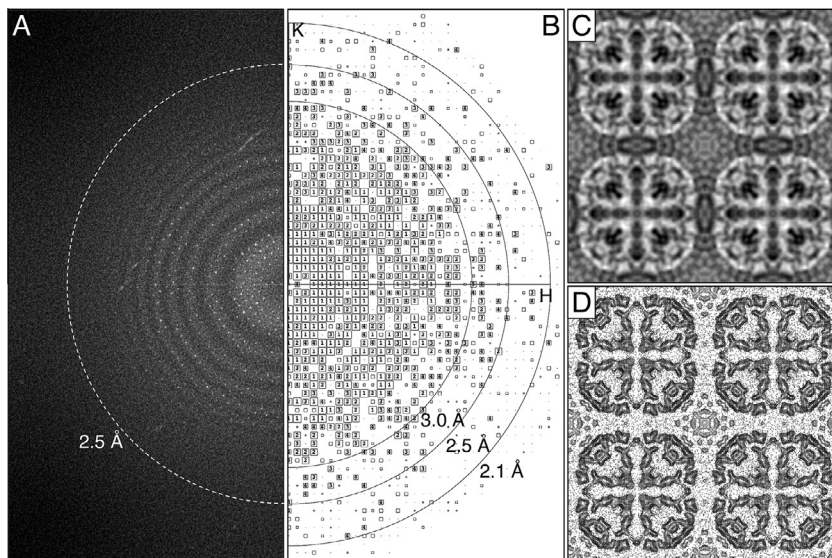


Fig. 2. Imaging of AQP0 2D crystals with a K2 Summit camera mounted on an FEI Polara electron microscope operated at 300 kV. (A) The power spectrum of a typical drift-corrected image recorded at a calibrated magnification of 50,926 \times after binning over 2×2 pixels shows Thon rings to a resolution of about 2.5 Å (indicated by dashed ring). (B) The IQ plot of a typical AQP0 2D crystal after lattice unbending shows IQ = 3 spots to a resolution of about 2.3 Å. (C) Projection map of AQP0 at 2.6 Å resolution obtained by merging the best seven images. (D) Projection map shown as contour plot. Panels C and D show four AQP0 unit cells, each with a side length of $a = b = 65.5$ Å.

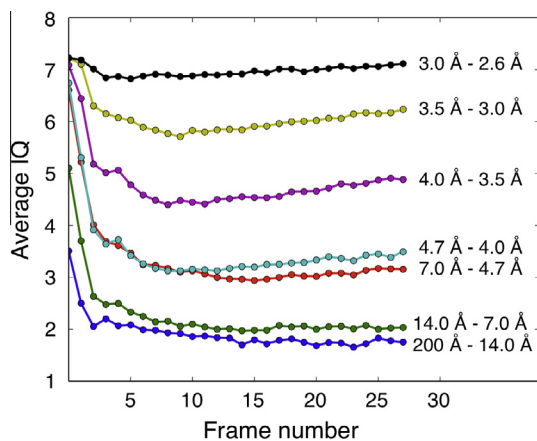


Fig. 3. Analysis of the effect of increasing electron dose on the average IQ values of diffraction spots in resolution bins. The average IQ values were calculated for the indicated resolution ranges and plotted against the cumulative frame number.

2013; Veesler et al., 2013). Dose-fractionated image stacks were recorded at liquid-nitrogen temperature at a calibrated magnification of 50,926 \times , giving physical and super-resolution pixel sizes of 0.98 and 0.49 Å on the specimen level, respectively. After 2×2 binning, the power spectra of motion-corrected images showed Thon rings to about 2.5 Å resolution (Fig. 2A) and IQ-3 diffraction spots to about 2.3 Å resolution (Fig. 2B). After lattice unbending, the best seven images were merged, and the phase residuals suggest a resolution of 2.6 Å resolution (Supplementary Table 2), close to about 3/4 of the physical Nyquist frequency of $1/(1.96 \text{ Å})$. The merged projection map at 2.6 Å resolution is shown in Fig. 2C and D.

In comparison, electron diffraction patterns we recorded previously from the same crystals showed reflections to a resolution beyond 2.0 Å. It is well known that electron diffraction patterns of 2D crystals often show diffraction spots to a resolution higher than those seen in images of the same crystals. Therefore, the resolution of images collected from 2D crystals is not limited by the intrinsic disorder in the crystals but rather by other factors, such

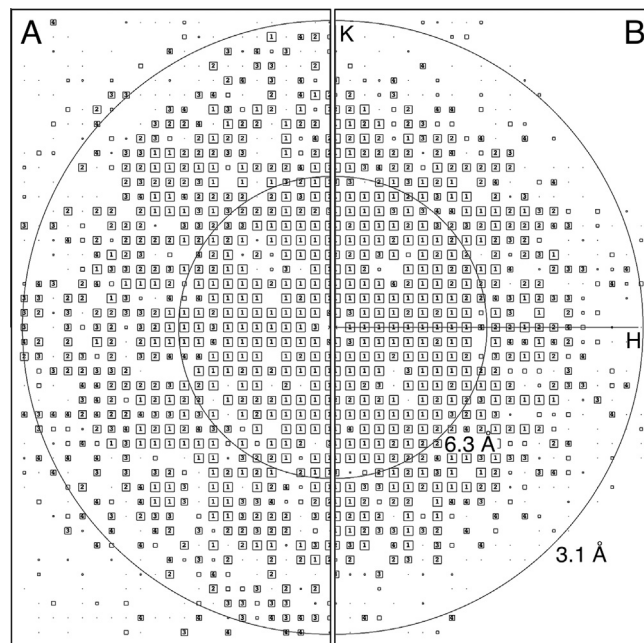


Fig. 4. Information beyond the physical Nyquist frequency. (A) AQP0 2D crystals were imaged with a K2 Summit camera mounted on an FEI Tecnai F20 electron microscope in super-resolution mode at a calibrated magnification of 40,410 \times , and the drift-corrected images were binned over 2×2 pixels. As the physical Nyquist frequency is $1/(2.48 \text{ Å})$, all reflections seen in the IQ plot are below the physical Nyquist frequency and within the normal resolution range. (B) AQP0 2D crystals were also imaged at a magnification of 15,858 \times , and the drift-corrected images were not binned. As the physical Nyquist frequency is $1/(6.3 \text{ Å})$, all reflections seen in the IQ plot beyond this resolution are above the physical Nyquist frequency and in the super-resolution range.

as specimen drift and beam-induced motions (Henderson and Glaeser, 1985; Glaeser et al., 2011). The results presented here demonstrate that the high DQE of the K2 camera together with computational motion correction make it possible to collect images of 2D crystals closer to the resolution limit imposed by the crystal order. However, even the use of a K2 camera and motion correction

will not correct for the very fast initial motion that occurs when the beam first illuminates the specimen, which can be minimized by the use of thick support carbon (Glaeser et al., 2011) or simply by removing the first one or two frames of the movie. It is also encouraging that images recorded with a Tecnai F20 electron microscope operated at 200 kV could be merged to 3.4 Å resolution, suggesting that even a modest microscope can be used for near-atomic resolution cryo-EM studies. It is not entirely clear why images collected on the Polara produced better results than those taken on the Tecnai F20. However, the Polara has a more stable specimen stage, and its enclosed design may shield the sample from high-frequency vibrations resulting from acoustic noise. While the motion-correction algorithm we are currently using may suffice to correct drift-like motion caused by stage instability, the 0.15-second subframe integration time will not allow correction for most sample vibrations caused by acoustic noise.

3.2. Assessment of the signal-to-noise ratio over the exposure time

Biological specimens are sensitive to radiation damage. Exposure to the electron beam thus gradually deteriorates the structural information, especially in the high-resolution range (Breedlove and Trammell, 1970; Glaeser, 1971). As a result, the intensity of diffraction spots and their SNR decrease with increasing exposure time and electron dose (Taylor and Glaeser, 1976). As the electron-counting K2 Summit camera allows for dose fractionation, it is possible to follow changes in the power spectrum with increasing electron dose. By using the binned super-resolution dataset of the AQP0 2D crystals recorded on the Tecnai F20, we analyzed the average IQ values within resolution bins as a function of the number of averaged movie frames. Since the IQ value measures the peak-to-background ratio of a reflection (Henderson et al., 1986), changes in the average IQ value in a given resolution bin

Table 1

Phase residuals in resolution shells. Images were taken on a K2 Summit DDD camera mounted on an F20 electron microscope in super-resolution mode at a magnification of 40,410× with subsequent binning over 2 × 2 pixels and at a magnification of 15,858× without binning. The phase residuals are given for separately merging seven images from each imaging condition (40 k, 2 × 2 binned and 16 k, unbinned), and for merging of all 14 images (combined). For each resolution shell the phase residual (in degree, top number) and number of spots (bottom number) are given. The red lines indicate the resolution cut-off (~80° phase residual) and the blue line indicates the physical Nyquist frequency for the images taken at a magnification of 15,858×.

#	DMIN DMAX		40k, 2x2 binned		16k, unbinned		combined	
			all IQs	IQ-wght	all IQs	IQ-wght	all IQs	IQ-wght
1	1000.0	11.6	23.1	17.9	22.3	19.4	29.3	22.4
1			323	323	329	329	652	652
2	11.6	8.2	26.1	21.9	27.3	24.1	29.0	24.0
2			329	329	328	328	657	657
3	8.2	6.7	27.9	25.0	21.7	18.8	25.6	23.1
3			346	346	347	347	693	693
4	6.7	5.8	40.9	36.4	39.5	34.0	42.2	37.3
4			346	346	342	342	688	688
5	5.8	5.2	27.9	24.1	27.0	21.3	27.6	23.6
5			317	317	319	319	636	636
6	5.2	4.7	41.9	31.6	40.2	30.7	42.9	33.1
6			312	312	274	274	586	586
7	4.7	4.4	36.0	32.6	39.0	36.6	39.7	35.8
7			335	335	322	322	657	657
8	4.4	4.1	39.8	31.6	52.0	44.4	44.0	35.8
8			309	309	264	264	573	573
9	4.1	3.9	55.4	47.2	63.0	57.7	61.7	52.4
9			265	265	224	224	501	501
10	3.9	3.7	56.3	47.1	77.6	72.7	62.1	53.0
10			317	317	238	238	584	584
11	3.7	3.5	64.2	57.0	70.9	68.4	68.6	59.2
11			281	281	178	178	487	487
12	3.5	3.4	78.3	76.3	80.5	70.7	79.9	75.1
12			178	178	143	143	407	407
13	3.4	3.2	76.8	79.4	85.6	87.5	83.3	82.7
13			166	166	135	135	429	429
14	3.2	3.1	78.0	73.3	95.8	90.7	89.4	87.4
14			85	85	85	85	308	308
15	3.1	3.0	80.2	73.5	73.6	70.9	83.4	80.1
15			67	67	39	39	294	294
Overall: Phase residual			44.112		45.546		49.046	
Number of spots			3976		3567		8152	

represent changes in the average SNR of reflections in that resolution bin.

Fig. 3 shows the average IQ values plotted against the number of averaged movie frames in different resolution bins (each frame corresponds to an electron dose of $0.78 \text{ counts}/\text{\AA}^2$). In the lower resolution bins (below a resolution of 4.7 \AA), the average IQ values initially decrease rapidly but then stabilize, indicating that averaging the first few frames improves the SNR whereas adding further frames does not further improve the SNR in these low-resolution bins. In the higher resolution bins (resolution between 4.7 and 3.0 \AA), the average IQ values also initially decrease rapidly but keep decreasing slowly to about frame 9, from which point on they begin to slowly increase. This behavior suggests that while the SNR improves initially with the addition of frames, from frame 9 onwards beam damage deteriorates the high-resolution information and leads to a decrease in the SNR. While the effect is small and may not be of practical relevance, the same trend can be seen in all three resolution bins. The average IQ values in the highest resolution bin (resolution between 3.0 and 2.6 \AA) are always close to 7, which means that the peaks equal the background level, so that the reflections in this resolution range do not contain meaningful information (Henderson et al., 1986).

3.3. Information beyond the physical Nyquist frequency in super-resolution mode

To address the question whether centroiding alters the phase information, we compared images of AQP0 2D crystals recorded at different magnifications, which thus have different pixel sizes and Nyquist frequencies. The AQP0 2D crystals used in this study diffract to high resolution and generate a sufficient number of diffraction spots for this analysis. In addition to data collected on the Tecnai F20 at a calibrated magnification of $40,410\times$ (an IQ plot of a typical motion-corrected image after lattice unbending is shown in Fig. 4A), we collected another set of dose-fractionated image stacks of AQP0 2D crystals at the lower calibrated magnification of $15,858\times$, giving a physical pixel size of 3.15 \AA on the specimen level, corresponding to a physical Nyquist frequency of $1/(6.3 \text{ \AA})$. All information beyond 6.3 \AA will therefore be in the super-resolution range (an IQ plot of a typical motion-corrected image after lattice unbending is shown in Fig. 4B). For optimal performance of the K2 Summit camera and the motion-correction algorithm, the dose rate was kept low, using $10 \text{ counts}/\text{pixel}/\text{s}$ ($1.036 \text{ counts}/\text{\AA}^2/\text{s}$; $2.5 \text{ counts}/\text{pixel}/\text{s}$ in super resolution), which is only slightly higher than the dose rate used at higher magnification ($8 \text{ counts}/\text{pixel}/\text{s}$; $5.203 \text{ counts}/\text{\AA}^2/\text{s}$). In order to ensure that the frames had sufficient SNR for subsequent motion correction, the frame read-out rate was adjusted to 400 ms per frame. The dose-fractionated image stacks were recorded with a total electron dose similar to the total dose used for the high-magnification dataset.

The dose-fractionated image stacks were not binned to retain the super-resolution information. After motion correction, the imaged crystals were computationally unbent, and the best seven images were merged. To determine the resolution to which the phase information is reliable, phase residuals were calculated in resolution bins for all spots with IQ values 1 to 8 (“all IQs” in the Tables) as well as phase residuals that were weighted by IQ value as implemented in the *2dx* software (Gipson et al., 2007b) (“IQ-wght” in the Tables). The images collected at the lower magnification could be merged to 3.4 \AA resolution (Table 1, middle; Supplementary Table 3), similar to those collected at the higher magnification after binning over 2×2 pixels (also 3.4 \AA resolution; Table 1, left; Supplementary Table 1), demonstrating that the phase information within each group is consistent to this resolution. When the unbinned images from the low-magnification

dataset were merged with the 2×2 binned images from the high-magnification dataset, the phases remained consistent to 3.4 \AA resolution (Table 1, right; Supplementary Table 4). This result shows that the data collected between 6.3 and 3.4 \AA , which lie in the super-resolution range for the images collected at the lower magnification, are consistent with the information in the same resolution range that is within physical Nyquist when collected at the higher magnification. Importantly, this indicates that super-resolution yields high-quality phase data that are directly useful for structure determination.

The results presented here suggest that it is possible to fully utilize the super-resolution pixels for structure determination. Recording images at lower magnifications may not be desirable for single-particle cryo-EM of small molecules, due to the lower DQE at frequencies beyond the Nyquist limit. It will become useful, however, for recording single-particle cryo-EM images of very large particles, such as large icosahedral viruses, for imaging 2D crystals larger than $1 \mu\text{m}$ in size, as well as for collecting electron tomographic data.

3.4. Influence of dose rate on image quality

We have previously reported that higher dose rates result in increased coincidence loss that affects the amplitude in the low-frequency region of power spectra (Li et al., 2013a). To assess the effect of different dose rates on image quality, we collected dose-fractionated image stacks of AQP0 2D crystals in super-resolution mode at different dose rates, but keeping the total electron dose the same.

The images were collected at a magnification of $15,858\times$, corresponding to a physical Nyquist frequency of $1/(6.3 \text{ \AA})$, using dose rates of 4, 8, and $20 \text{ counts}/\text{pixel}/\text{s}$. The dose rate was measured at the camera level after the specimen was inserted, and gain and dark references were carefully prepared after the dose rate was set. To end up with the same total electron dose of $20 \text{ counts}/\text{\AA}^2$ per image stack and to ensure that the individual frames have a sufficient SNR for subsequent motion correction, the frame read-out times were adjusted, resulting in different exposure times. For the dose rate of $4 \text{ counts}/\text{pixel}/\text{s}$, 120 frames were recorded at 400 ms per frame, giving an exposure time of 48 s ; for the dose rate of $8 \text{ counts}/\text{pixel}/\text{s}$, 120 frames were recorded at 200 ms per frame, an exposure time of 24 s ; and for

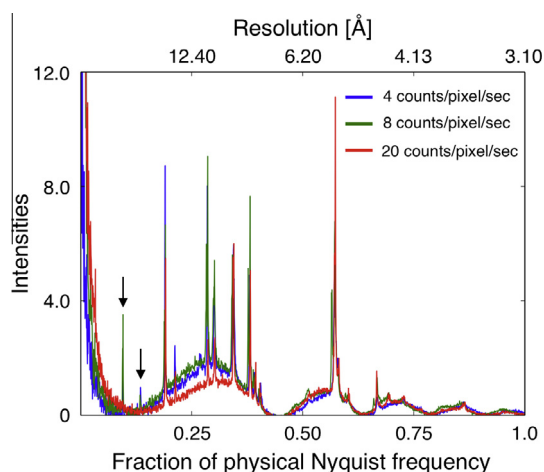


Fig. 5. Radial averages of power spectra calculated from representative images recorded with different dose rates. Diffraction spots in the low-resolution range are clearly seen in the images recorded with dose rates of 4 and $8 \text{ counts}/\text{pixel}/\text{s}$ (arrows). By contrast, due to the greater coincidence loss, these diffraction spots are no longer detectable in the image recorded with a dose rate of $20 \text{ counts}/\text{pixel}/\text{s}$.

the dose rate of 20 counts/pixel/s, 128 frames were recorded at 75 ms per frame, yielding an exposure time of 9.6 s.

Power spectra and IQ plots of motion-corrected images recorded with all three dose rates showed diffraction spots to a resolution of about 3.5 Å (Supplementary Fig. 1). We first calculated one-dimensional rotational averages of the power spectra of representative images recorded at the three different dose rates at approximately the same defocus (Fig. 5). While intensities for diffraction spots at a resolution below 0.2 of the physical Nyquist frequency are clearly observed for the images recorded with 4 and 8 counts/pixel/s (arrows in Fig. 5), these intensities are missing in the image recorded with 20 counts/pixel/s. Thus, at a dose rate

of 20 counts/pixel/s, coincidence loss results in sufficient dampening of the amplitudes in the lower resolution range that low-order reflections are no longer visible above the background (Li et al., 2013a; Ruskin et al., 2013). For each dataset, the best seven images were then merged, and the phase residuals are shown in Table 2 and Supplementary Tables 5–7. All datasets could be merged individually to about 3.5 Å resolution, and the behavior of the phase residuals within each dataset as a function of resolution is similar for the three datasets (Fig. 6A). We note that the phase residuals in the different resolution bins of data recorded with 8 counts/pixel/s are consistently better than those of data recorded with 4 and 20 counts/pixel/s. In particular, although data recorded at a dose

Table 2

Phase residuals in resolution shells. Images were taken on a K2 Summit DDD camera mounted on an F20 electron microscope in super-resolution mode at a magnification of 15,858 \times without binning using dose rates of 4, 8 and 20 counts/pixel/s. The phase residuals are given for separately merging seven images from each imaging condition. For each resolution shell the phase residual (in degree, top number) and number of spots (bottom number) are given. The red lines indicate the resolution cut-off ($\sim 80^\circ$ phase residual).

#	DMIN DMAX		4 counts/pixel/s		8 counts/pixel/s		20 counts/pixel/s	
			all IQs	IQ-wght	all IQs	IQ-wght	all IQs	IQ-wght
1	1000.0	13.4	13.5	11.6	21.9	18.4	19.4	16.6
1			234	234	237	237	236	236
2	13.4	9.5	25.2	22.8	21.1	20.0	26.9	22.4
2			259	259	265	265	259	259
3	9.5	7.7	21.7	20.7	25.9	23.5	26.0	24.4
3			263	263	262	262	261	261
4	7.7	6.7	22.5	17.9	22.3	19.4	23.4	18.9
4			245	245	250	250	243	243
5	6.7	6.0	31.6	24.5	30.2	26.8	35.9	30.8
5			253	253	258	258	255	255
6	6.0	5.5	25.9	20.8	24.7	20.7	29.8	21.3
6			209	209	212	212	201	201
7	5.5	5.1	29.6	19.6	27.2	20.4	34.6	25.9
7			265	265	261	261	253	253
8	5.1	4.7	38.2	28.4	37.1	29.3	40.7	31.4
8			224	224	242	242	213	213
9	4.7	4.5	37.8	32.8	37.3	30.6	44.2	38.6
9			237	237	259	259	233	233
10	4.5	4.2	46.1	32.9	41.1	33.0	55.8	40.1
10			206	206	228	228	208	208
11	4.2	4.0	53.3	43.9	56.3	43.1	65.2	47.1
11			197	197	219	219	185	185
12	4.0	3.9	64.8	55.8	57.4	46.2	80.5	75.6
12			129	129	148	148	134	134
13	3.9	3.7	68.6	60.7	63.8	50.0	81.5	74.6
13			196	196	215	215	178	178
14	3.7	3.6	78.8	69.4	74.6	68.6	86.2	80.9
14			141	141	155	155	138	138
15	3.6	3.5	94.7	88.6	80.1	71.5	89.8	80.9
15			123	123	120	120	120	120
16	3.5	3.4	89.7	87.2	83.7	77.0	89.5	79.9
16			137	137	149	149	146	146
17	3.4	3.3	99.2	100.1	92.2	85.1	102.2	95.0
17			133	133	142	142	129	129
18	3.3	3.2	88.4	82.6	86.3	85.0	93.3	88.0
18			111	111	136	136	117	117
Overall:	Phase residual		44.787		43.719		50.079	
	Number of spots		3562		3758		3509	

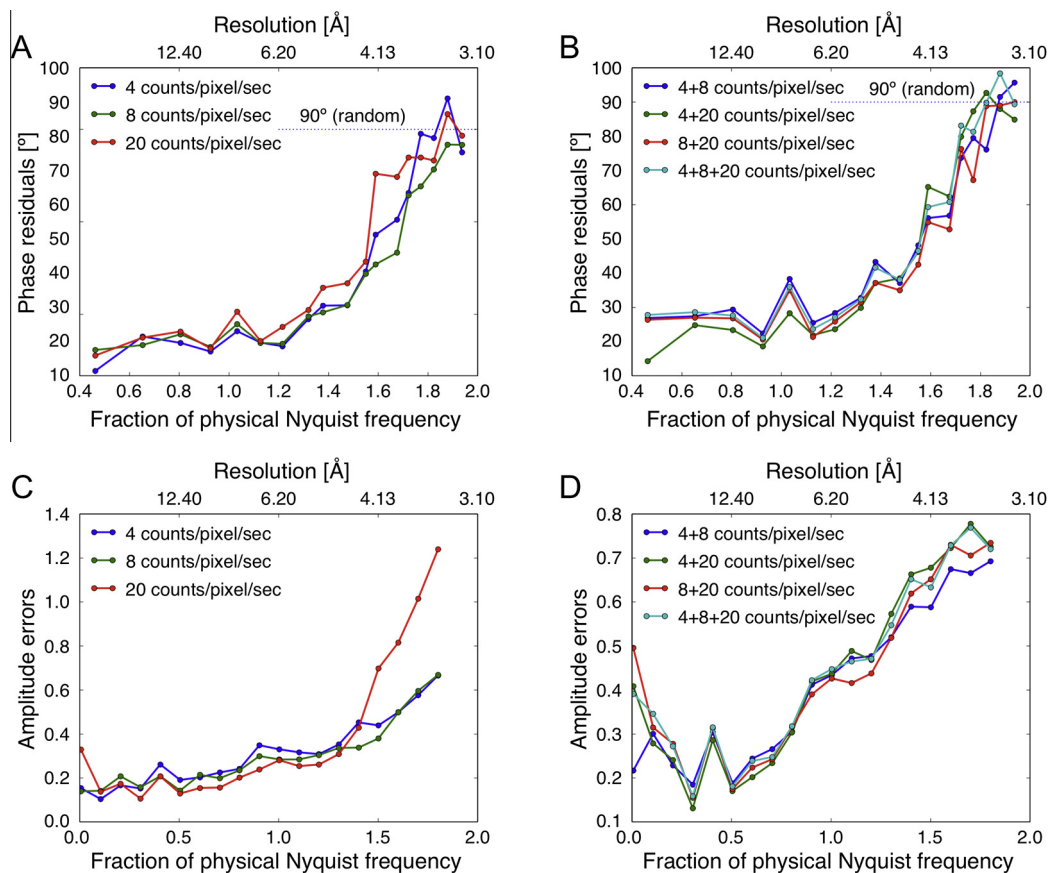


Fig. 6. Influence of dose rate on phase and amplitude information. AQP0 2D crystals were imaged with a K2 Summit camera mounted on an FEI Tecnai F20 electron microscope in super-resolution mode at a calibrated magnification of 15,858 \times , corresponding to a physical Nyquist frequency of 1/(6.3 Å), using dose rates of 4, 8, and 20 counts/pixel/s. (A) and (C) Plots of phase residuals and amplitude errors as a function of spatial frequency for merging of the best seven images recorded with the different dose rates. (B) and (D) The same plots but for the merging of image sets that were recorded with different dose rates.

rate of 4 counts/pixel/s should be better compared to the other two datasets, the phase residuals are somewhat higher, which may be caused by the longer frame read-out time that was used (400 ms instead of 150 ms). This will limit the effectiveness of motion correction, especially for data collected with an electron microscope equipped with a side-entry specimen stage such as the Tecnai F20. Still, our results indicate that for dose rates ranging from 4 to 20 counts/pixel/s, the phase information in images for each group is consistent to a resolution of about 3.5 Å. Furthermore, an analysis of the number of spots with given IQ values shows that their distribution is similar for all three datasets in all resolution ranges (Supplementary Fig. 2). This result is in agreement with the previous finding that different dose rates do not affect the SNR of images recorded with the same total electron dose.

To compare the phase quality between data recorded at different dose rates, different datasets were merged with each other, i.e., data recorded at 4 counts/pixel/s with data recorded at 8 counts/pixel/s, data recorded at 4 counts/pixel/s with data recorded at 20 counts/pixel/s, data recorded at 4 counts/pixel/s with data recorded at 20 counts/pixel/s, as well as all the data. The resulting phase residual statistics show that the data recorded at different dose rates are all consistent to about 3.5 Å resolution (Table 3), and plots of phase residual against spatial frequency show similar trends for all merged datasets (Fig. 6B). Thus, the phase information is consistent between datasets irrespective of what dose rate was used. Interestingly, there is a small increase in phase residual at the resolution corresponding to the physical Nyquist frequency. While this increase is small, $\sim 15^\circ$, it was observed for all datasets.

The datasets recorded at different dose rates were also used to assess the effect of dose rate on the amplitude information

(Fig. 6C). Comparison of the amplitude errors in resolution bins shows that the data recorded with 4 and 8 counts/pixel/s are comparable. For data recorded with 20 counts/pixel/s, the amplitude error is higher in the lowest resolution bin (below 62.0 Å or 0.2 of the physical Nyquist frequency), which can be explained by the higher coincidence loss at higher dose rates. However, the amplitude error is also significantly higher in the high-resolution bins (above 4.13 Å or 1.5 times the physical Nyquist frequency). A dose rate of 20 counts/pixel/s not only increases coincidence losses (which influences mostly low resolution region), but also reduces modulation transfer function (MTF) and DQE at both high and low frequencies, which can be explained by the higher coincidence loss at higher dose rates. The large amplitude errors in the high-resolution range may be attributed to the lower DQE of the K2 Summit camera in this range at higher dose rates (Li et al., 2013a; Ruskin et al., 2013).

When images recorded with different dose rates were merged (Fig. 6D), the amplitude errors of all datasets including the images recorded with 20 counts/pixel/s increased substantially in the low-resolution range (below 62.0 Å) but not as much in the high-resolution range (above 4.13 Å). In addition, all combined datasets show a peak of high amplitude error at a resolution of about 15 Å (Fig. 6D, arrow), which appears less prominent in individual datasets (Fig. 6C, arrow). Compared to the phase information, the amplitude information appears to be much more affected by coincidence loss that is caused by higher dose rates.

It is widely accepted in the X-ray crystallography field that phase information is far more important for the reconstruction of a 3D electron density map than the amplitude information. Moreover, image amplitudes are greatly modulated by the contrast

Table 3

Phase residuals in resolution shells. Images were taken on a K2 Summit DDD camera mounted on an F20 electron microscope in super-resolution mode at a magnification of 15,858 \times without binning using dose rates of 4, 8 and 20 counts/pixel/s. The phase residuals are given for merging combinations of seven images each of the indicated imaging conditions. For each resolution shell the phase residual (in degree, top number) and number of spots (bottom number) are given. The red lines indicate the resolution cut-off ($\sim 80^\circ$ phase residual).

#	DMIN DMAX		4+8 counts/pixel/s		4+20 counts/pixel/s		8+20 counts/pixel/s		4+8+20 counts/pixel/s	
			all IQs	IQ-wght	all IQs	IQ-wght	all IQs	IQ-wght	all IQs	IQ-wght
1	1000.0	13.4	30.7	26.9	16.7	14.3	31.4	26.4	31.4	27.8
1			471	471	470	470	473	473	707	707
2	13.4	9.5	29.4	27.4	28.9	24.8	30.7	27.0	32.0	28.6
2			524	524	518	518	524	524	783	783
3	9.5	7.7	31.3	29.4	24.7	23.4	28.9	26.8	29.4	27.6
3			525	525	524	524	523	523	786	786
4	7.7	6.7	25.7	22.4	23.4	18.6	24.1	20.6	24.8	21.1
4			495	495	488	488	493	493	738	738
5	6.7	6.0	41.2	38.3	34.3	28.3	38.2	35.0	39.4	36.0
5			511	511	508	508	513	513	766	766
6	6.0	5.5	29.7	25.5	28.9	21.9	27.6	21.4	29.1	23.7
6			421	421	410	410	413	413	622	622
7	5.5	5.1	35.1	28.4	32.4	23.6	33.2	25.9	34.3	27.1
7			526	526	518	518	514	514	779	779
8	5.1	4.7	40.9	32.8	39.9	29.9	39.8	31.5	40.8	32.4
8			466	466	437	437	455	455	679	679
9	4.7	4.5	47.5	43.3	41.8	37.1	44.6	37.2	46.9	41.6
9			496	496	470	470	492	492	729	729
10	4.5	4.2	48.3	37.1	52.4	38.5	48.2	35.0	51.2	38.1
10			434	434	414	414	436	436	642	642
11	4.2	4.0	61.5	48.1	58.2	46.2	59.4	42.5	60.5	46.5
11			416	416	382	382	404	404	601	601
12	4.0	3.9	65.0	56.1	72.0	65.2	67.9	54.9	68.1	59.3
12			277	277	263	263	282	282	367	367
13	3.9	3.7	67.7	56.8	71.7	62.4	67.1	52.8	71.2	60.8
13			411	411	374	374	393	393	513	513
14	3.7	3.6	78.3	73.7	79.8	79.9	78.5	76.3	80.6	83.1
14			296	296	279	279	293	293	365	365
15	3.6	3.5	87.0	79.5	95.7	87.3	82.7	67.2	87.6	81.3
15			243	243	243	243	240	240	309	309
16	3.5	3.4	83.5	76.1	90.4	92.7	87.6	88.8	87.6	89.8
16			286	286	283	283	295	295	358	358
17	3.4	3.3	91.1	91.5	93.2	88.0	90.1	89.0	94.8	98.4
17			275	275	262	262	271	271	338	338
18	3.3	3.2	92.6	95.7	90.5	84.9	88.8	90.0	90.5	89.4
18			247	247	228	228	253	253	303	303
Overall: Phase residual			49.469		47.539		48.459		48.493	
Number of spots			7320		7071		7267		10385	

transfer function (CTF), which complicates the accurate measurement of amplitudes. Our results indicate that the coincidence loss created by higher dose rates leads to a decrease in the measured amplitudes but does not systematically alter phases, suggesting that image reconstruction is still feasible under dose rate conditions that create greater coincidence loss.

Above all, when it is desirable to have a larger field of view, say with large 2D crystals, it is feasible to set up data collection at lower magnifications, as long as dose rates are kept in the same $<10 e^-/s$ regime. It may also be useful to increase the read-out rate to improve motion correction, but at the expense of significantly

expanded data sizes. Hence, the magnification and the subframe integration time should be carefully chosen for image data collection.

3.5. Influence of dose fractionation protocol on image deterioration

The recording of dose-fractionated image stacks to enable correction of beam-induced specimen motion has become the standard procedure for data collection (Bai et al., 2013; Campbell et al., 2012; Li et al., 2013a). A study of beam-induced motion revealed a pattern, in which motion is larger in the beginning of

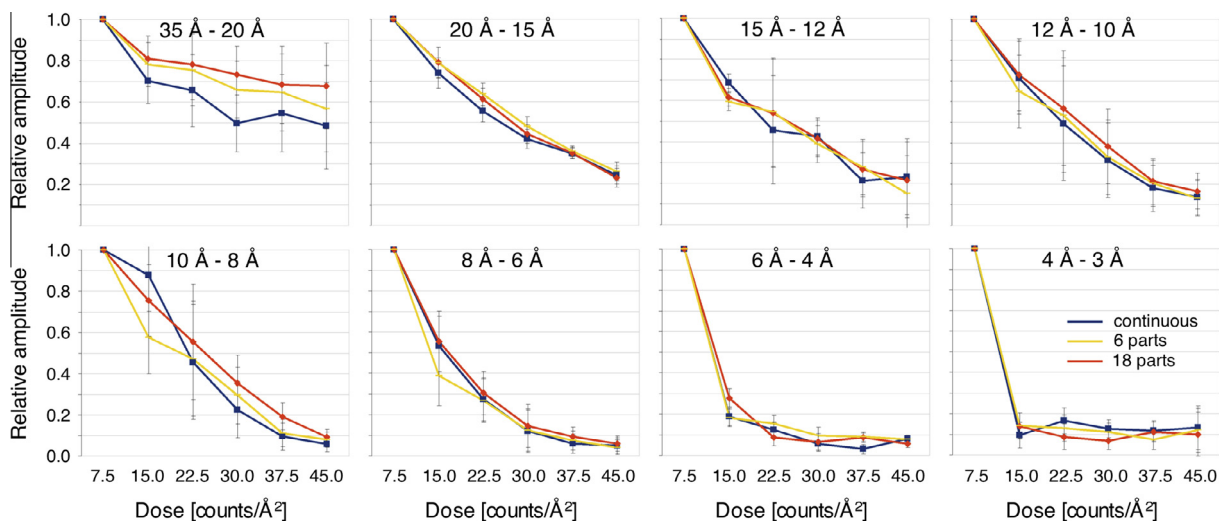


Fig. 7. Effect of different dose fractionation protocols on beam damage. AQP0 2D crystals were imaged with a K2 Summit camera mounted on an FEI TF30 electron microscope in super-resolution mode at a calibrated magnification of $50,637\times$, using a total dose of $45\text{ counts}/\text{\AA}^2$ but three different protocols: image stacks recorded without interruption (continuous), image stacks recorded in six exposures separated by $\sim 30\text{ s}$ pauses (6 parts), and image stacks recorded in 18 exposures separated by $\sim 15\text{ s}$ pauses (18 parts). The plots show the amplitudes measured at different total applied electron doses for different resolution ranges.

an exposure and then slows down (Brilot et al., 2012). The reason for this pattern is not known but may point to an annealing mechanism that relaxes strain present in the amorphous ice layer and carbon support. When the beam is turned off and back on after a pause of 60 s, a motion pattern similar to the initial exposure is observed, including initial motions of similar magnitude (Brilot et al., 2012). Only after several repeated exposures a significant reduction of motion is observed. It is therefore possible that different dose fractionation time courses may lead to different motion patterns. Using the K2 Summit camera, we recorded image stacks of AQP0 2D crystals in super-resolution mode with a total dose of $45\text{ counts}/\text{\AA}^2$ and a dose rate of $20\text{ counts}/\text{pixel}/\text{s}$. Three protocols were tested and compared: image stacks recorded without interruption (continuous), image stacks recorded in six exposures separated by $\sim 30\text{ s}$ pauses (6 parts) and image stacks recorded in 18 exposures separated by $\sim 15\text{ s}$ pauses (18 parts). For all exposure series, we kept the sample drift rate below $2\text{ \AA}/\text{s}$ and chose a beam diameter that significantly exceeded the field of view. This ensured that unexposed parts of the crystal moving into the beam between exposures did not affect our measurements.

Fig. 7 shows plots of amplitudes measured at different total applied electron doses. After dividing the data into different resolution bins it can be seen that the dose sensitivity is greatest for the highest resolution and least for the lowest resolution, as observed previously (Glaeser, 1971). The plots suggest that the image amplitudes, which are indicative of the structural integrity of the crystals, decay at the same rate (within measurement error) for all three data collection protocols tested. The underlying cause of beam-induced motion remains uncertain but may include specimen charging and the build-up of internal pressure due to molecular radicals generated by radiolysis (Glaeser, 2008). Our observation that different fractionation protocols can lead to the same loss of structural integrity but different motion trajectories suggest that either radiation damage is not the sole cause of the sample motion, or the damage caused by the beam continues for a certain time after the beam has been switched off.

In conclusion, our current studies demonstrate that electron counting and centroiding used by the K2 Summit camera does not affect the phase information in the super-resolution range beyond the physical Nyquist frequency. Thus, it is possible to record images at a lower magnification to fully utilize the total

number of super-resolution pixels. Furthermore, at least up to a dose rate of $20\text{ counts}/\text{pixel}/\text{s}$, the influence of coincidence loss on phase information, if there is any, may be negligible.

Acknowledgments

This work was supported in part by HHMI (to D.A.A.), NSF grant DBI-0960271 (to D.A.A and Y.C.), which in part funded the development of the K2 camera in association with Gatan and Peter Denes at Lawrence Berkeley Labs, NIH grants R01 GM082893 (to Y.C.), R01 GM098672 (to Y.C.), P01 GM62580 (to N.G. and T.W.), R01 GM031627 (to D.A.A.) and P50 GM082250 (to A. Frankel). D.A.A., N.G. and T.W. are investigators with the Howard Hughes Medical Institute.

Appendix A. Supplementary data

Supplementary data associated with this article can be found, in the online version, at <http://dx.doi.org/10.1016/j.jsb.2015.08.015>.

References

- Allegretti, M., Mills, D.J., McMullan, G., Kuhlbrandt, W., Vonck, J., 2014. Atomic model of the F420-reducing [NiFe] hydrogenase by electron cryo-microscopy using a direct electron detector. *Elife* 3, e01963.
- Amunts, A., Brown, A., Bai, X.C., Llacer, J.L., Hussain, T., Emsley, P., Long, F., Murshudov, G., Scheres, S.H., Ramakrishnan, V., 2014. Structure of the yeast mitochondrial large ribosomal subunit. *Science* 343, 1485–1489.
- Bai, X.C., Fernandez, I.S., McMullan, G., Scheres, S.H., 2013. Ribosome structures to near-atomic resolution from thirty thousand cryo-EM particles. *Elife* 2, e00461.
- Bammes, B.E., Rochat, R.H., Jakana, J., Chen, D.H., Chiu, W., 2012. Direct electron detection yields cryo-EM reconstructions at resolutions beyond $3/4$ Nyquist frequency. *J. Struct. Biol.* 177, 589–601.
- Bartesaghi, A., Merk, A., Banerjee, S., Matthies, D., Wu, X., Milne, J.L., Subramaniam, S., 2015. 2.2 \AA resolution cryo-EM structure of β -galactosidase in complex with a cell-permeant inhibitor. *Science* 348, 1147–1151.
- Breedlove Jr., J.R., Trammell, G.T., 1970. Molecular microscopy: fundamental limitations. *Science* 170, 1310–1313.
- Brilot, A.F., Chen, J.Z., Cheng, A., Pan, J., Harrison, S.C., Potter, C.S., Carragher, B., Henderson, R., Grigorieff, N., 2012. Beam-induced motion of vitrified specimen on holey carbon film. *J. Struct. Biol.* 177, 630–637.
- Campbell, M.G., Cheng, A., Brilot, A.F., Moeller, A., Lyumkis, D., Veleser, D., Pan, J., Harrison, S.C., Potter, C.S., Carragher, B., Grigorieff, N., 2012. Movies of ice-embedded particles enhance resolution in electron cryo-microscopy. *Structure* 20, 1823–1828.

- Crowther, R.A., Henderson, R., Smith, J.M., 1996. MRC image processing programs. *J. Struct. Biol.* 116, 9–16.
- Faruqi, A.R., McMullan, G., 2011. Electronic detectors for electron microscopy. *Q. Rev. Biophys.* 44, 357–390.
- Gipson, B., Zeng, X., Zhang, Z.Y., Stahlberg, H., 2007a. 2dx – user-friendly image processing for 2D crystals. *J. Struct. Biol.* 157, 64–72.
- Gipson, B., Zeng, X., Stahlberg, H., 2007b. 2dx_merge: data management and merging for 2D crystal images. *J. Struct. Biol.* 160, 375–384.
- Glaeser, R.M., 1971. Limitations to significant information in biological electron microscopy as a result of radiation damage. *J. Ultrastruct. Res.* 36, 466–482.
- Glaeser, R.M., 2008. Retrospective: radiation damage and its associated “information limitations”. *J. Struct. Biol.* 163, 271–276.
- Glaeser, R.M., McMullan, G., Faruqi, A.R., Henderson, R., 2011. Images of paraffin monolayer crystals with perfect contrast: minimization of beam-induced specimen motion. *Ultramicroscopy* 111, 90–100.
- Gonen, T., Sliz, P., Kistler, J., Cheng, Y., Walz, T., 2004. Aquaporin-0 membrane junctions reveal the structure of a closed water pore. *Nature* 429, 193–197.
- Gonen, T., Cheng, Y., Sliz, P., Hiroaki, Y., Fujiyoshi, Y., Harrison, S.C., Walz, T., 2005. Lipid-protein interactions in double-layered two-dimensional AQP0 crystals. *Nature* 438, 633–638.
- Gyobu, N., Tani, K., Hiroaki, Y., Kamegawa, A., Mitsuoka, K., Fujiyoshi, Y., 2004. Improved specimen preparation for cryo-electron microscopy using a symmetric carbon sandwich technique. *J. Struct. Biol.* 146, 325–333.
- Henderson, R., Glaeser, R.M., 1985. Quantitative analysis of image contrast in electron micrographs of beam-sensitive crystals. *Ultramicroscopy* 16, 139–150.
- Henderson, R., Baldwin, J.M., Downing, K.H., Lepault, J., Zemlin, F., 1986. Structure of purple membrane from halobacterium halobium: recording, measurement and evaluation of electron micrographs at 3.5 Å resolution. *Ultramicroscopy* 19, 147–178.
- Hite, R.K., Li, Z., Walz, T., 2010a. Principles of membrane protein interactions with annular lipids deduced from aquaporin-0 2D crystals. *EMBO J.* 29, 1652–1658.
- Hite, R.K., Schenk, A.D., Li, Z., Cheng, Y., Walz, T., 2010b. Collecting electron crystallographic data of two-dimensional protein crystals. *Methods Enzymol.* 481, 251–282.
- Li, X., Mooney, P., Zheng, S., Booth, C.R., Braunfeld, M.B., Gubbens, S., Agard, D.A., Cheng, Y., 2013a. Electron counting and beam-induced motion correction enable near-atomic-resolution single-particle cryo-EM. *Nat. Methods* 10, 584–590.
- Li, X., Zheng, S.Q., Egami, K., Agard, D.A., Cheng, Y., 2013b. Influence of electron dose rate on electron counting images recorded with the K2 camera. *J. Struct. Biol.* 184, 251–260.
- Liao, M., Cao, E., Julius, D., Cheng, Y., 2013. Structure of the TRPV1 ion channel determined by electron cryo-microscopy. *Nature* 504, 107–112.
- McMullan, G., Clark, A.T., Turchetta, R., Faruqi, A.R., 2009a. Enhanced imaging in low dose electron microscopy using electron counting. *Ultramicroscopy* 109, 1411–1416.
- McMullan, G., Chen, S., Henderson, R., Faruqi, A.R., 2009b. Detective quantum efficiency of electron area detectors in electron microscopy. *Ultramicroscopy* 109, 1126–1143.
- McMullan, G., Faruqi, A.R., Clare, D., Henderson, R., 2014. Comparison of optimal performance at 300keV of three direct electron detectors for use in low dose electron microscopy. *Ultramicroscopy* 147, 156–163.
- Milazzo, A.C., Cheng, A., Moeller, A., Lyumkis, D., Jacovetty, E., Polukas, J., Ellisman, M.H., Xuong, N.H., Carragher, B., Potter, C.S., 2011. Initial evaluation of a direct detection device detector for single particle cryo-electron microscopy. *J. Struct. Biol.* 176, 404–408.
- Mindell, J.A., Grigorieff, N., 2003. Accurate determination of local defocus and specimen tilt in electron microscopy. *J. Struct. Biol.* 142, 334–347.
- Ruskin, R.S., Yu, Z., Grigorieff, N., 2013. Quantitative characterization of electron detectors for transmission electron microscopy. *J. Struct. Biol.* 184, 385–393.
- Shroff, H., Galbraith, C.G., Galbraith, J.A., White, H., Gillette, J., Olenych, S., Davidson, M.W., Betzig, E., 2007. Dual-color superresolution imaging of genetically expressed probes within individual adhesion complexes. *Proc. Natl. Acad. Sci. U. S. A.* 104, 20308–20313.
- Taylor, K.A., Glaeser, R.M., 1976. Electron microscopy of frozen hydrated biological specimens. *J. Ultrastruct. Res.* 55, 448–456.
- Veesler, D., Campbell, M.G., Cheng, A., Fu, C.Y., Murez, Z., Johnson, J.E., Potter, C.S., Carragher, B., 2013. Maximizing the potential of electron cryomicroscopy data collected using direct detectors. *J. Struct. Biol.* 184, 193–202.
- Zhang, X., Zhou, Z.H., 2011. Limiting factors in atomic resolution cryo electron microscopy: no simple tricks. *J. Struct. Biol.* 175, 253–263.